Water Incorporation Mechanisms and Effects in $MgSiO_3$-majorite Under High Temperature and Pressure Conditions

Yancheng Lou[1,2,3,*], Zhigang Zhang[3,4], Andrew M. Walker[5], Stephen Stackhouse[6], Meng Chen[1,2], and Hongping He[1,2,4]

[1]State Key Laboratory of Deep Earth Processes and Resources, Guangzhou Institute of Geochemistry, Chinese Academy of Sciences, Guangzhou, 510640, China.

[2]Guangdong Research Center for Strategic Metals and Green Utilization, Guangzhou, 510640, China.

[3]Key Laboratory of Planetary Science and Frontier Technology, Institute of Geology and Geophysics, Chinese Academy of Sciences, Beijing 100029, China.

[4]College of Earth and Planetary Sciences, University of Chinese Academy of Sciences, Beijing 100049, China.

[5]Department of Earth Sciences, University of Oxford, South Park Road, Oxford OX1 3AN, United Kingdom.

[6]School of Earth and Environment, University of Leeds, Leeds LS2 9JT, United Kingdom.

Corresponding author: Yancheng Lou (louyancheng@gig.ac.cn)

Key Points:

- The dominant water incorporation mechanisms in $MgSiO_3$-majorite are the two types of tetrahedral hydrous defects.
- The impact of the two dominant tetrahedral hydrous defects on the elastic properties of $MgSiO_3$-majorite are significantly different.
- In $MgSiO_3$-majorite, water incorporation exhibits a greater effect on S-wave than on P-wave velocities under high-pressure conditions.

* Corresponding author: louyancheng@gig.ac.cn

Abstract

The incorporation of water in high-pressure minerals is essential for the water cycle within the interiors of terrestrial planets. Majoritic garnet, a major component in the mantles of Earth and Mars, plays a significant role in this context. In this study, we use first-principles simulations to explore water incorporation mechanisms in $MgSiO_3$-majorite, which is a key end-member of majoritic garnet, at conditions up to 2000 K and 20 GPa. By dealing with the relationship between chemical potential and the Gibbs free energy changes for the reactions at equilibrium conditions, we determine the ratios of the seven potential hydrous defects. Our results reveal that the Si2 and Si3 defects, which are of the hydrogarnet-type, dominate water incorporation in $MgSiO_3$-majorite. In addition, we evaluate the effects of these hydrous defects on seismic wave velocities. The presence of Si2 and Si3 defects, with an expected water concentration of ~700 ppm, has a small effect on both P-wave and S-wave velocities. Nevertheless, the influence of water on lateral variations in the seismic wave velocities of $MgSiO_3$-majorite, which is opposite to that found for ringwoodite, offers a potential tool for investigating compositional heterogeneities in hydrated regions of planetary mantles.

Plain Language Summary

Water in high-pressure minerals makes up a significant component of deep water in terrestrial planets and plays an important role in their planetary water cycles. Constraining how water is stored in majoritic garnet, a major mineral in the mantles of Earth and Mars, is important for understanding how water is stored and moves in these environments. In this study, we explore how water is incorporated into $MgSiO_3$-majorite, a key end-member of majoritic garnet, under high-pressure and high-temperature conditions. Based on extensive first-principles simulations, we find that two types of tetrahedral hydrous defects are the main ways water is stored in $MgSiO_3$-majorite. These defects have a small effect on the seismic velocities of $MgSiO_3$-majorite at an expected water concentration of ~700 ppm. However, they exhibit a stronger influence on S-wave than on P-wave velocities, which is similar to the behavior observed in wadsleyite but different from that in ringwoodite. This characteristic may help us to better understand compositional heterogeneities in hydrated regions of planetary mantles.

1 Introduction

Water is important for shaping the evolution of terrestrial planets such as Earth and Mars (Bell & Rossman, 1992; Bolfan-Casanova, 2005; Nestola & Smyth, 2016; Ni et al., 2017; Ohtani, 2020; Pearson et al., 2014; Peslier et al., 2017; Smyth & Jacobsen, 2006). The presence of water can significantly affect the melting point, wave speed, thermal conductivity, electrical conductivity, and other properties of minerals (Faccenda, 2014; Mao & Li, 2016; B. Zhang & Xia, 2021). In view of this, it is necessary to investigate the mechanism of water incorporation in high-pressure minerals, to better understand the influence of water.

Majoritic garnet, the high-pressure phase of garnet, is a major component in the mantles of Earth and Mars (van der Lee, 2023; Yoshizaki & McDonough, 2020, 2021). It is the second most abundant component (up to ~40 mol.%; Frost, 2008; Yoshizaki & McDonough, 2021) in the Earth's mantle transition zone (MTZ) and the major component (up to ~90 mol.%; Smith et al.,

2018; Stixrude & Lithgow-Bertelloni, 2012) in cold slabs at Earth's MTZ depth. In the mantle of Mars, it is the second most abundant component (up to ~40 mol.%; Yoshizaki & McDonough, 2020, 2021) at depths of about 1000-1800 km. Majoritic garnet not only plays significant roles in many geodynamic processes, but also acts as an important reservoir and carrier of water in the deep interiors of these planets (Scambelluri et al., 2008; van Mierlo et al., 2013).

$MgSiO_3$-majorite (space group: $I4_1/a$, abbreviated as Mgmj hereafter) is a key silicon-rich end-member of majoritic garnet (Akaogi & Akimoto, 1977; Angel et al., 1989; Irifune, 1987; Irifunea & Ringwood, 1987; Ringwood, 1967, 1991). As shown in Fig.1, its crystal structure features seven types of polyhedrons, marked as Mg1-3 and Si1-4, which is more than other garnet end-members because of the occupation of octahedral sites by equal amounts of Si^{4+} and Mg^{2+} instead of trivalent cations. Mg1 and Mg2 polyhedrons are dodecahedrons which are distinguished by distortion relative to the cube (Mg1 is more distorted than Mg2). Mg3 and Si4 are octahedrons whose main difference is the type of central cations. Si1, Si2, and Si3 are tetrahedrons which mainly differ in their bonding environment, they connect with four Mg octahedrons, four Si octahedrons, and two Mg and two Si octahedrons, respectively. These polyhedrons provide multiple possible incorporation mechanisms for water because hydrous defects (hydroxyl point defects) in nominally anhydrous minerals, which are generated by the substitution of H for metal cations minerals, are the main storage mechanism of water (Bell & Rossman, 1992; Hirschmann & Kohlstedt, 2012; Inoue et al., 1998; Jacobsen, Jiang, et al., 2008; Manghnani et al., 2005; Mao et al., 2011; Peslier et al., 2017; Walker et al., 2007; Wang et al., 2006).

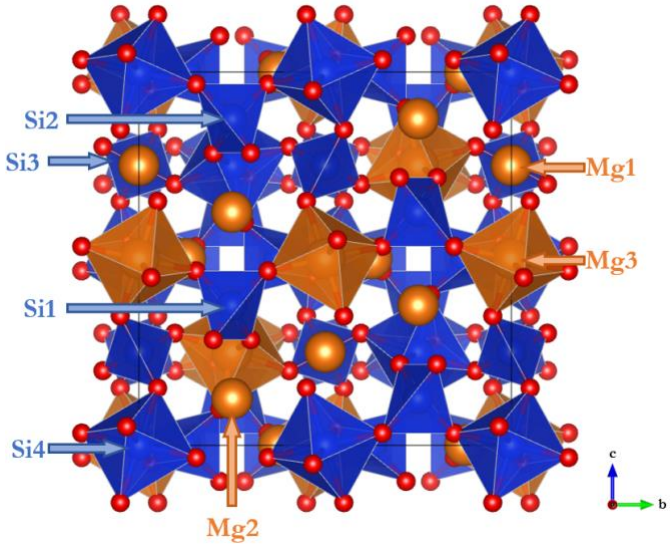

Figure 1. Unit cell of $MgSiO_3$-majorite, which is a tetragonal structure (space group: $I4_1/a$) with 160 atoms ($Mg_{32}Si_{32}O_{96}$) and includes eight $Mg_3(Mg,Si)[SiO_4]_3$ units. Red balls represent O^{2-}; Orange balls represent Mg^{2+} (the exposed balls represent Mg^{2+} in Mg1 and Mg2 dodecahedral sites, the balls in orange octahedrons represent Mg^{2+} in Mg3 sites); Blue balls represent Si^{4+} (the balls in blue tetrahedrons and octahedrons represent Si^{4+} in Si1-3 and Si4 sites, respectively).

Previous studies of water incorporation mechanisms in Mgmj are limited to static results (Pigott et al., 2015), which found the Si2 hydrous defect to be the dominant water incorporation mechanism at MTZ pressures. This type of hydrous defect, together with Si1 and Si3 defects, where four hydrogen atoms replace a silicon atom in a tetrahedral site, are known as "hydrogarnet defects" (Cohen-Addad et al., 1967) and are common in natural garnets and other minerals at relatively low temperatures (Balan et al., 2011; Blanchard et al., 2009; Qin et al., 2018; Wright et al., 1994). There is even a complete solid solution sequence called hydrogrossular, $Ca_3Al_2(SiO_4)_{3-x}(OH)_{4x}$, in which all the Si tetrahedrons become hydrous defects (Adhikari et al., 2017; Rossman & Aines, 1991). However, the water incorporation mechanism may change at higher temperatures, as found for other mantle minerals. For instance, the main water incorporation mechanism of forsterite changes from Si tetrahedral defects to Mg octahedral defects with increasing temperature (Qin et al., 2018; Walker et al., 2007). Motivated by these previous studies, we deployed first-principles simulations of Mgmj and inspected its seven potential hydrous defects up to 2000 K and 20 GPa. By solving the equations for the chemical potential and the Gibbs free energy changes for the reactions at equilibrium conditions, we obtained their ratios that quantify the main incorporation mechanisms of water. In addition, we further calculated the elastic properties of dry and hydrous Mgmj to show the impact of hydrous defects on its physical properties and discussed the implications of our results.

2 Methods and computational details

In order to understand the distribution of hydrogen between the different types of possible hydrous defect in Mgmj, we need a model for the free energy change of reactions amongst the defect types and data on the relative enthalpy and entropy of the defects. We first introduce our model of reactions before describing the atomic scale approach we use to investigate individual defects.

2.1 Reaction model

Since Mgmj has seven types of cation site, the incorporation of water may involve equilibria among these potential cation defects and water. To avoid the difficulty of directly modeling the energetics of supercritical water, we evaluate the relative stability of every pair of defect mechanisms by the following reactions (Pigott et al., 2015):

$$\text{R1: } Mg_{32N}Si_{32N-1}O_{96N}H_4(\text{Si1}) + SiO_2 = Mg_{32N-2}Si_{32N}O_{96N}H_4(\text{Mg1}) + 2MgO$$

$$\text{R2: } Mg_{32N}Si_{32N-1}O_{96N}H_4(\text{Si2}) + SiO_2 = Mg_{32N-2}Si_{32N}O_{96N}H_4(\text{Mg2}) + 2MgO$$

$$\text{R3: } Mg_{32N}Si_{32N-1}O_{96N}H_4(\text{Si1}) + SiO_2 = Mg_{32N-2}Si_{32N}O_{96N}H_4(\text{Mg3}) + 2MgO$$

$$\text{R4: } Mg_{32N-2}Si_{32N}O_{96N}H_4(\text{Mg2}) + 2MgO = Mg_{32N}Si_{32N-1}O_{96N}H_4(\text{Si1}) + SiO_2$$

$$\text{R5: } Mg_{32N-2}Si_{32N}O_{96N}H_4(\text{Mg3}) + 2MgO = Mg_{32N}Si_{32N-1}O_{96N}H_4(\text{Si2}) + SiO_2$$

$$\text{R6: } Mg_{32N-2}Si_{32N}O_{96N}H_4(\text{Mg3}) + 2MgO = Mg_{32N}Si_{32N-1}O_{96N}H_4(\text{Si3}) + SiO_2$$

$$\text{R7: } Mg_{32N-2}Si_{32N}O_{96N}H_4(\text{Mg3}) + 2MgO = Mg_{32N}Si_{32N-1}O_{96N}H_4(\text{Si4}) + SiO_2$$

where the symbols Mg1-3 and Si1-4 represent corresponding hydrous defects in Mgmj, the N represents the number of unit cells of dry Mgmj corresponding to the hydrous Mgmj phases, the phase MgO is periclase, the phase SiO_2 is alpha-quartz at 0 K and 0 GPa but stishovite at 0 K and 10 and 20 GPa as well as at 2000 K and ~20 GPa. We treat MgO and SiO_2 as precipitates and

consider the other reactants and products of hydrous Mgmj phases as a solid binary mixture, which means their chemical potential are (Levine, 2009):

$$\mu_i = \mu_i^* + RT\ln x_i\gamma_i \quad (1)$$

where μ_i is the chemical potential of component i with mole fraction x_i at temperature T and pressure P, R represent the gas constant, γ_i represent the activity coefficient which can be treated as 1 because of the similar structure between hydrous Mgmj phases, and μ_i^* is the chemical potential of pure i (phase of hydrous Mgmj) at the same temperature and pressure. For reactions above, taking R1 as an example, we have:

$$\Delta_r G = \sum \upsilon_i \mu_i^* + RT\ln \frac{x_{\mathrm{Mg1}}}{x_{\mathrm{Si1}}} \quad (2)$$

where $\Delta_r G$ is the Gibbs free energy change of reaction, υ_i is the stoichiometric number, the subscripts of Mg1 and Si1 represent the phase of hydrous Mgmj with two Mg1 hydrous defects and one Si1 hydrous defect, respectively. $\sum \upsilon_i \mu_i^*$ can be given by:

$$\sum \upsilon_i \mu_i^* = \sum \upsilon_i [H_i^* - T(S_{i,\mathrm{vib.}}^* + S_{i,\mathrm{conf.}}^*)] \quad (3)$$

where H_i^* is the enthalpy of pure i, which is obtained as $U + pV$ from molecular dynamics within the NVT ensemble. Here, U is the ensemble-averaged internal energy, p is target pressure (rather than the ensemble-averaged pressure, as explained in Section S1.2), and V is the volume, which is constant. Notably, the enthalpy of the pure hydrous Mgmj phase with different water concentrations ($H^*_{\mathrm{hydrous\ Mgmj}}$) is calculated from the enthalpy of pure Mgmj (H^*_{Mgmj}) and the hydration enthalpy ($\Delta H_{i,\mathrm{hydration}}$, which is the enthalpy difference between dry and hydrous mineral phases arising from one hydrous defect, i.e., $H^*_{i(\mathrm{hydrous\ Mgmj\ with\ one\ hydrous\ defect})} - NH^*_{\mathrm{Mgmj}}$ here, N has the same meaning as in R1-7), which is described in Section S1.2. $S_{i,\mathrm{vib.}}^*$ and $S_{i,\mathrm{conf.}}^*$ are the vibrational and configurational entropy of pure i, respectively. The former is expected to be very small and can be ignored (Muir & Brodholt, 2018; Qin et al., 2018), the latter for each phase in each reaction can be calculated from Boltzmann's entropy formula:

$$S_{i,\mathrm{conf.}}^* = k_B \ln W_{i,\mathrm{conf.}} \quad (4)$$

where k_B is Boltzmann constant, $W_{\mathrm{conf.}}$ represents the number of possible configurations of the hydrous defect which can be calculated from $W_{i,\mathrm{conf.}} = C_{NV+NC}^{NV}(C_{NH+NE}^{NH})^{NV}$, where NV represents the number of defect vacancies (i.e., hydrous defects), NC represents the number of polyhedrons containing the original cation, NH represents the number of O^{2-} bonded to H^+ in vacancies and NE represents the number of O^{2-} which are not bonded to H^+. It is obvious that this equation consists of two parts: C_{NV+NC}^{NV} is the contribution of vacancies in the lattice and $(C_{NH+NE}^{NH})^{NV}$ is the contribution of H^+ in vacancies. Due to the large number of atoms involved the former is simplified using the Stirling approximation ($\ln A! \approx A(\ln A - 1)$). For a system made of N_h unit cell of hydrous Mgmj (e.g., $Mg_{32N}Si_{32N-1}O_{96N}H_4$(Si1) in R1), assuming nv hydrous defects and nc polyhedrons containing the original cation in a unit cell (i.e., $N_hV = N_hnv$, $N_hC = N_hnc$), the $S_{i,\mathrm{conf.}}^*$ for one unit cell can be estimated by:

$$S_{i,\mathrm{conf.}}^* = k_B \ln[C_{NV+NC}^{NV}(C_{NH+NE}^{NH})^{NV}]/N_h$$

$$= \frac{k_B \ln C_{NV+NC}^{NV}}{N_h} + \frac{k_B \ln (C_{NH+NE}^{NH})^{NV}}{N_h}$$

$$= \frac{k_B[(NV+NC)\ln(NV+NC) - NV\ln(NV) - NC\ln(NC)]}{N_h} + k_B\ln(C_{NH+NE}^{NH})^{nv}$$

$$= k_B[(nv+nc)\ln(nv+nc) - nv\ln(nv) - nc\ln(nc)] + k_B\ln(C_{NH+NE}^{NH})^{nv} \quad (5)$$

Then, at the condition of equilibrium for a balanced chemical reaction, i.e., $\Delta_r G = 0$, the Eqn. (2) can be expressed as:

$$\sum v_i(H_i^* - TS_{i,\text{conf.}}^*) = -RT\ln\frac{x_{\text{Mg1}}}{x_{\text{Si1}}} \quad (6)$$

After solving simultaneously such equations for R1-7, we can obtain the equilibrium ratios of mole fractions of seven kinds of hydrous Mgmj phases. In the Supporting Information (Section S1.1 and S1.2), we provide more details of the calculation framework, including the estimation of the uncertainties of our results and other technical notes.

2.2 First-principles simulations

First-principles simulations, which are based on a quantum mechanical description of the electronic structure, are used to obtain the energy of mineral phases and the trajectories describing the atomic motion used in this study. All simulations were performed with the Vienna ab initio simulation package (VASP, Kresse and Hafner, 1993; Kresse and Furthmüller, 1996a, b; Kresse and Joubert, 1999) which is based on density functional theory (DFT, Hohenberg and Kohn, 1964; Kohn and Sham, 1965) and the projector augmented wave (PAW) approach (Blöchl, 1994; Kresse & Joubert, 1999). The PBE (Perdew et al., 1996) implementation of the generalized gradient approximation (GGA) to the exchange-correlation functional is used. Elements of Mg, Al, Si, O, and H are included in simulations (chemical formulae are detailed in Section 2.1). The core radii used by the PAW pseudopotentials were 1.06 Å for Mg ($2p^6 3s^2$, valence configuration with p semi-core valence state), 1.01 Å for Al ($2s^2 2p^1$), 0.79 Å for Si ($3s^2 3p^2$), 0.80 Å for O ($2s^2 2p^4$) and 0.58 Å for H ($1s^1$). Van der Waals corrections were not applied in this study, since according to tests by Muir and Brodholt (2018), the effect of van der Waals corrections on calculated geometry and water distribution are negligible based on their comparison between DFT-D3 (Grimme et al., 2010), DFT-TS (Tkatchenko & Scheffler, 2009) and non-D methods.

For the static simulations, the calculation parameters were: 800 eV for energy cutoff, 10^{-8} eV for energy convergence criterion, and 2×2×2 for the Brillouin zone sampling grid. Total energies calculated with these parameters are converged to within 0.2 meV/atom. We optimized the structure by minimizing the enthalpy at 0, 10, and 20 GPa. The high-temperature simulations were performed by using ab initio molecular dynamics (AIMD) simulations within the NVT ensemble with the Nosé thermostat (Nosé, 1984). The calculation parameters for them were: 500 eV for energy cutoff, 10^{-6} eV for energy convergence criterion, and 1×1×1 for the Brillouin zone sampling grid (Γ-point). Total energies calculated with these parameters converged to within 1.0 meV/atom. Tests show that the difference in energy obtained using a time-step, of 0.5 and 1 fs, are within 1.0 meV/atom and could be ignored (Table S2). Hence, each 2000 K simulation of dry and hydrous Mgmj included a 1 ps pre-equilibrium stage with a 0.5 fs time-step and a 12 ps equilibrium stage with a 1 fs time-step, and the systems reached equilibrium after ~2500 steps (Fig. S1). For other minerals with a smaller unit cell, and without hydrous defects, a series of AIMD simulations were used to obtain the 3rd-order Birch-Murnaghan equation of state (EOS) and the required properties

at the target pressure—the lack of hydrogen atoms meant that the simulation time could be shorter (6 ps).

Initial mineral structures are built using the open-source visualization software VESTA (Momma & Izumi, 2011) based on their space groups (Mgmj: Angel et al. (1989), alpha-quartz: Levien et al. (1980), stishovite: Ross et al. (1990), periclase: Jacobsen et al. (2008), forsterite: Hazen (1976), ringwoodite: Ye et al. (2012)) except for hydrous Mgmj. The starting structures for the seven kinds of hydrous Mgmj are obtained by introducing charge-balanced substitution of H^+ for cations in polyhedrons in dry Mgmj. The H^+ were positioned close to several types of the O^{2-} in polyhedrons based on previous static energetic simulations (Pigott et al., 2015). The pairing relationships between hydrogen and oxygen ions and the bonding environments of six types of oxygens are shown in Table 1. The location of hydrous defects in the lattice can be random, according to Muir and Brodholt (2018). Furthermore, defect-defect interactions caused by the periodic boundary conditions are considered negligible in this study as demonstrated in static calculations on hydrous Mgmj (Pigott et al., 2015). The initial structures of dry and hydrous Mgmj for 2000 K and ~20 GPa AIMD simulations are inherited from those optimized at static conditions and lower pressures (the impact of imprecise pressure can be corrected as mentioned in the Supplemental Section S1.2).

Table 1. The bonding environments of six types of oxygen ions in $MgSiO_3$-majorite. The number of "X" represents the number of oxygens in a polyhedron. H superscript indicates the initial matching relationships between O^{2-} and H^+ in polyhedron.

Ions	Mg1 (dod)	Mg2 (dod)	Mg3 (oct)	Si1 (tet)	Si2 (tet)	Si3 (tet)	Si4 (oct)
O1	X	XX	XX			X^H	
O2	X	XX				X^H	X^HX^H
O3	XX					X^H	X^HX^H
O4	XX^H		XX			X^H	
O5	X^H	X^HX^H	X^HX^H	$X^HX^HX^HX^H$			
O6	X	XX			$X^HX^HX^HX^H$		XX

3 Results

3.1 Hydration enthalpy and configurational entropy

$\Delta H_{i,\mathrm{hydration}}$ and $S^*_{i,\mathrm{conf.}}$ of the seven kinds of hydrous Mgmj are listed in Table 2, the $S^*_{i,\mathrm{conf.}}$ with water concentrations of < ~5600 ppm were determined at 2000 K because the upper limit of solubility of water in Mgmj is ~2200 ± 500 ppm (Thomas et al., 2015). There are notable differences in the $\Delta H_{i,\mathrm{hydration}}$ calculated at static conditions and 2000 K. This is because the range of motion of hydrogens is larger than that of other atoms in MD simulations, which typically causes a larger increase in the potential energy of hydrous Mgmj than that of dry Mgmj, consequently, $\Delta H_{i,\mathrm{hydration}}$ increases. The relative magnitude of seven $\Delta H_{i,\mathrm{hydration}}$ remains consistent from static to elevated temperatures. For Mg hydrous defects, the $\Delta H_{\mathrm{Mg1,hydration}}$ is the smallest, and its $S^*_{\mathrm{Mg1,conf.}}$ is the largest, making it the defect with the highest probability of occurrence. For Si hydrous defects, the $\Delta H_{\mathrm{Si2,hydration}}$ is the smallest (Fig. 2), however, its

250 $S^*_{\mathrm{Si2,conf.}}$ is not the largest (being smaller than that of Si3) at the water concentrations we considered.
251 The probability of occurrence depends on the temperature, which directly affects the contribution
252 of S to G (the $TS^*_{i,\mathrm{conf.}}$ term). As shown in Table 2, the $S^*_{\mathrm{Si3,conf.}}$ of Si3 hydrous defect are always
253 the largest among all Si hydrous defects at 2000 K. This makes its $\Delta G_{\mathrm{Si3,hydration}}$
254 ($\Delta H_{\mathrm{Si3,hydration}} + TS^*_{\mathrm{Si3,conf.}}$) is finally slightly smaller than that of Si2, resulting in the highest
255 probability of occurrence for the Si3 hydrous defect (Fig. 2b).

256 **Table 2.** $\Delta H_{i,\mathrm{hydration}}$ and $S^*_{i,\mathrm{conf.}}$ of seven kinds of hydrous Mgmj. SD represents standard
257 deviation at 2000 K and 20 GPa.

Hydrous defect	$\Delta H_{i,\mathrm{hydration}}$ (eV)					$S^*_{i,conf.}$ (eV/K for 4 H)				
	0 K			2000 K		Water concentration (ppm)				
	0 GPa	10 GPa	20 GPa	20 GPa	SD	~88 ppm	~700 ppm	~1400 ppm	~2800 ppm	~5600 ppm
Mg1	-1.48	-1.33	-1.29	-0.76	0.05	1.94E-03	1.58E-03	1.46E-03	1.34E-03	1.22E-03
Mg2	-1.20	-1.15	-1.25	-0.74	0.12	1.82E-03	1.46E-03	1.34E-03	1.22E-03	1.09E-03
Mg3	-1.18	-1.18	-1.30	-0.41	0.12	1.71E-03	1.35E-03	1.23E-03	1.11E-03	9.86E-04
Si1	-4.75	-4.46	-4.34	-2.49	0.07	6.24E-04	4.44E-04	3.83E-04	3.22E-04	2.60E-04
Si2	-5.55	-4.98	-4.70	-2.91	0.10	6.24E-04	4.44E-04	3.83E-04	3.22E-04	2.60E-04
Si3	-5.25	-4.75	-4.46	-2.68	0.08	7.43E-04	5.64E-04	5.04E-04	4.44E-04	3.83E-04
Si4	-4.72	-3.90	-3.08	-1.17	0.19	9.17E-04	7.37E-04	6.77E-04	6.17E-04	5.56E-04

258
259
260
261
262

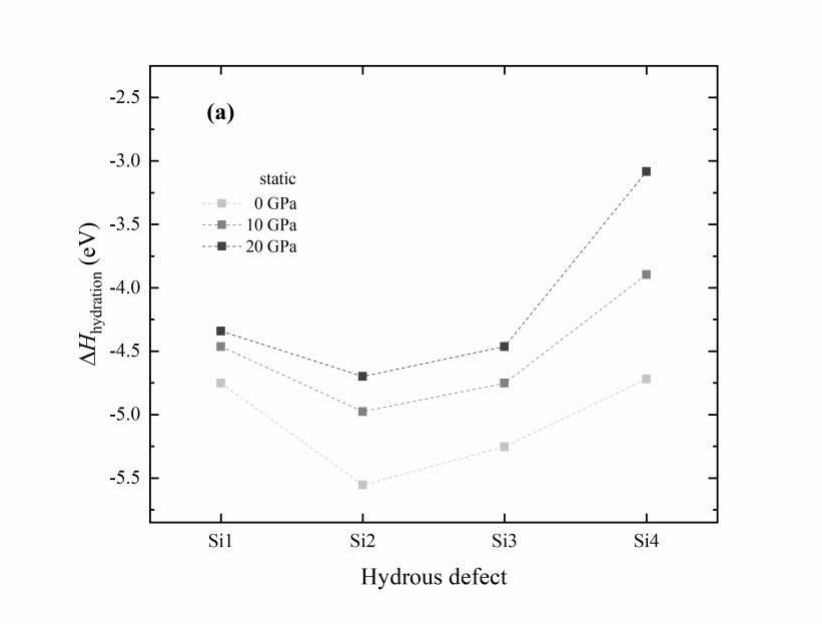

263

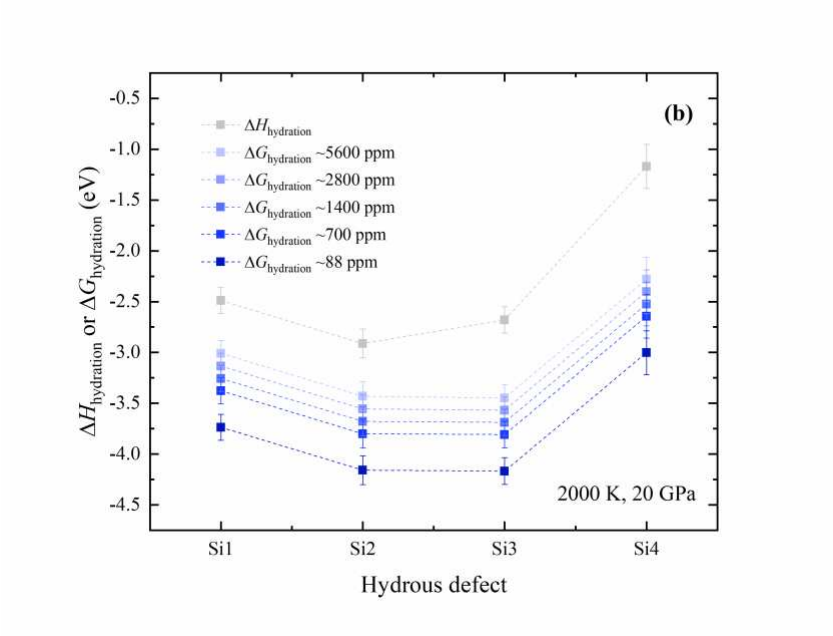

Figure 2. $\Delta H_{\mathrm{hydration}}$ and $\Delta G_{\mathrm{hydration}}$ of Si hydrous defects for (**a**) static, and (**b**) 2000 K and 20 GPa results.

3.2 Equilibria of Reactions

The comparison of occurrence probability between Mg and Si hydrous defects in Mgmj relies on the ΔG for R1-7. As shown in Fig. 3a, the tetrahedral Si2 hydrous defect is the most probable hydrous defect at 0 K with almost no pressure dependence. This observation is consistent with previous ambient experimental and static simulation studies of Mgmj and other garnet phases (Bolfan-Casanova et al., 2000; Geiger et al., 1991, 2000; Katayama et al., 2003; Pigott et al., 2015). However, the ratio of another tetrahedral defect, the Si3 hydrous defect, is remarkable at high temperatures compared to static results, and it becomes the most probable hydrous defect along with Si2 hydrous defect at 2000 K and 20 GPa (Fig. 3b) with weak dependence of water concentration (Fig.3c and d). Since the water incorporation mechanisms may be affected by the activity of SiO_2 (Lemaire et al., 2004; Matveev et al., 2001), we also calculated proportions of seven hydrous Mgmj for another set of reactions that do not contain SiO_2 (see R8-14 in Section S2.1). Comparing Fig. 3 and S3, the results seem to be quite similar, the most obvious difference is that the ratio and error of Mg1 at 88 ppm water concentration in Fig. 3c are a little larger than those in Fig S3c.

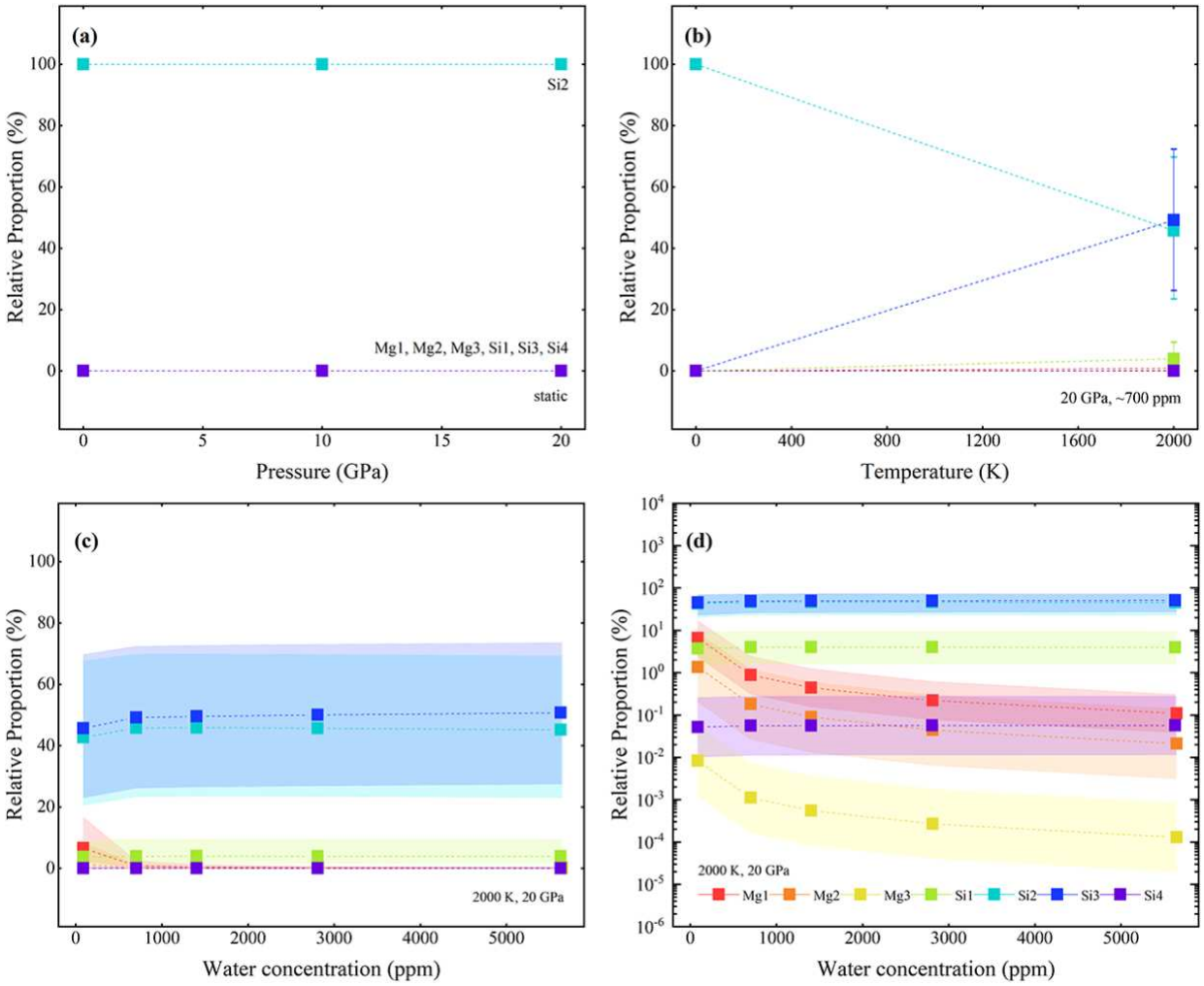

Figure 3. Relative proportions of seven kinds of hydrous Mgmj. (**a**) shows the pressure dependence at 0 K, (**b**) shows temperature dependence at 20 GPa, and (**c**) and (d) show water concentration dependence at 2000 K and 20 GPa in linear and logarithmic terms, respectively. The straight dashed lines connecting data points are guides to the eye. The confidence bands represent the estimated uncertainties in the values. Note that, except for the values for the Si2 and Si3 hydrous defects, the values for all other defects are in most cases indistinguishable from the values for the Si4 hydrous defect

4 Discussion

4.1 The main water incorporation mechanism in Mgmj

Our results show the dominance of Si2 and Si3 hydrous defects, while revealing the relatively small impact of pressure and water concentration on the ratios of hydrous defects. Although temperature has a more significant effect on the ratios, the trends of proportions of different hydrous defects with increasing temperature indicate that Si2 and Si3 remain predominant across the typical temperature range of Mgmj existence (T: ~1400-2000 K; Frost, 2008; Yoshizaki & McDonough, 2021). Notably, we observe binding preferences of H in hydrous defects with unsaturated pairings (i.e., Mg1, Mg2, Mg3, and Si4) in high-temperature simulations. However, this only reduces their ratios because the calculations of $S^*_{i,\mathrm{conf.}}$ assume equal binding probabilities between H and all oxygen atoms in polyhedrons. These binding preferences decreases the number of possible configurations, thereby reducing $S^*_{i,\mathrm{conf.}}$. Taking the Mg1 hydrous defect as an example, our estimation shows that when considering the binding preferences of H, the proportion of Mg1 hydrous defects decreases from ~6.8% to ~3.9% at a water concentration of ~88 ppm (the condition corresponding to the largest ratio of the Mg1 hydrous defect in our results). Detailed calculations provided in Section S2.2.

It should also be noted that the ratios of Mg hydrous defects in our results were derived from energy calculations of hydrous Mgmj phases containing only one type of Mg hydrous defects, without considering combinations of different Mg hydrous defect types. To address this, we calculated the configurational entropy of mixed Mg hydrous defects based on the ratios of the three Mg hydrous defects (Table S3, Fig. 3c and 3d), and estimated the proportion of hydrous Mgmj phases containing three types of Mg defect at 2000 K, ~20 GPa, and a water concentration of ~88 ppm conditions. The results, which do not consider binding preferences of H, show that its proportion (~12.3%) is larger than the sum of proportions of three types of hydrous Mgmj phase containing only one type of Mg hydrous defects (~8.12%). However, this difference does not affect the dominance of Si2 and Si3 defects within common water concentration ranges, i.e., at least ≥ 100 ppm (Section S2.3).Therefore, based on the analyses above, Si2 and Si3 hydrous defects seem to be the dominant water incorporation mechanisms in Mgmj at the conditions where Mgmj exists in the mantle (P: ~10-25 GPa; T: ~1400-2000 K; Frost, 2008; Yoshizaki & McDonough, 2021).

4.2 The effects of hydrous defects

The properties of hydrous Mgmj are related to the type of hydrous defects. Therefore, we compare the structure and bonding environment of three kinds of tetrahedron defects, which mainly involves two aspects, due to their expected dominance (especially Si2 and Si3) in hydrous Mgmj. The first is the types of connected octahedrons. Si1 tetrahedrons connect to four Mg octahedrons, Si2 tetrahedrons connect to four Si octahedrons, and Si3 tetrahedrons connect to two Mg octahedrons and two Si octahedrons. As shown in Table S1, the impact of a Si octahedron on the volume of Mgmj by the formation of a Si tetrahedron defect is greater than that of a Mg octahedron. In addition, the increase in the volume in hydrous Mgmj with one Si2 hydrous defect compared to dry Mgmj (about 0.86%, 0.41%, 0.22% for 0 K and 0, 10, 20 GPa, respectively) is about twice than that of Si1 (about 0.42%, 0.20%, 0.08% for 0 K and 0, 10, 20 GPa, respectively). The second is the orientation of the bonding structure. The spatial configuration of the bonding structure of Si tetrahedrons (one Si tetrahedron bonded to four octahedrons) in Mgmj is plane-like,

i.e., longer in two directions and shorter in the third vertical direction (see examples in Fig. 4a, b, and c). The orientation of the planar structure for Si1 and Si2 tetrahedrons are in the direction of the c-axis, but Si3 is in the direction of the a- or b-axis (Fig. 4d).

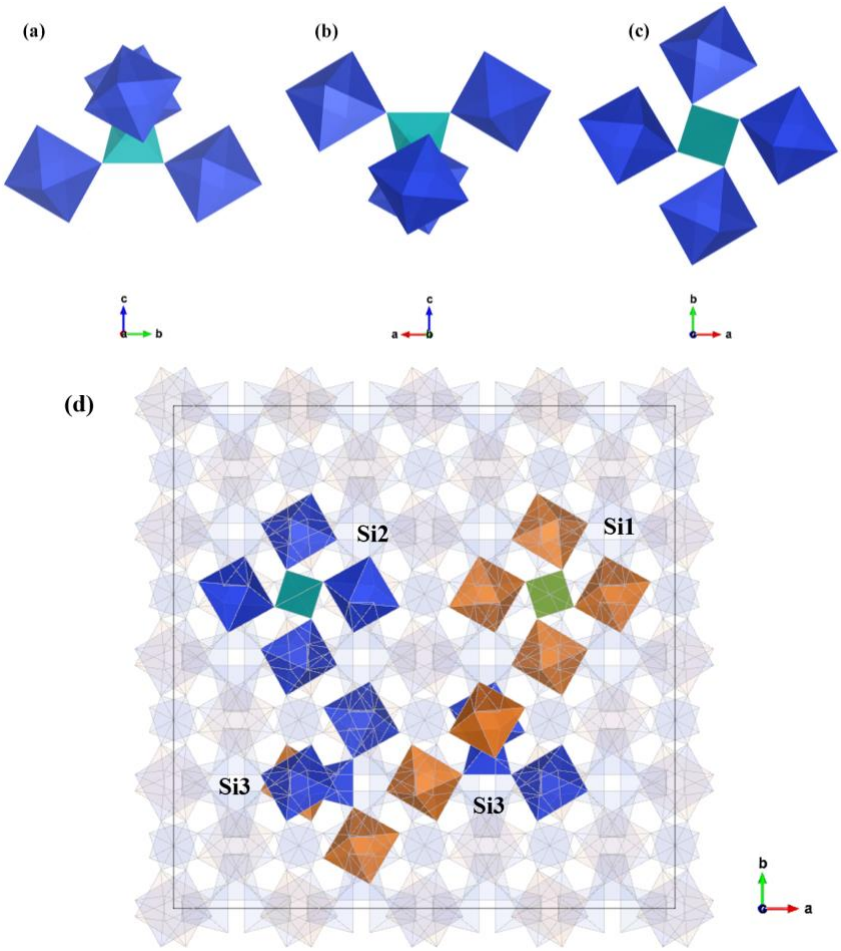

Figure 4. Sample Si tetrahedron (Si2) bonding environment: (a) front view, (b) right view, and (c) top view. And (d) is the top view of three types of sample Si tetrahedrons in a 2x2x2 supercell of Mgmj. The green tetrahedron connected with four Mg octahedrons (orange) represents Si1 tetrahedron, the cyan tetrahedron connected with four Si octahedrons (blue) represents Si2 tetrahedron, and the blue tetrahedron connected with two Mg octahedrons and two Si octahedrons represents Si3 tetrahedron. For clarity, other unrelated polyhedrons are made transparent and the Mg atoms in dodecahedrons are not shown.

According to the above analysis, these three defects exert different influences on the strain of hydrous Mgmj which may be reflected in some physical properties, such as shear mechanical properties. To demonstrate this, the static seismic wave velocities for Mgmj with or without Si defects were calculated to enable comparison. The method for calculating the elastic properties followed previous studies (Lou et al., 2020; Z. Zhang et al., 2013), a detailed description is in Section S1.3. As shown in Fig. 5, S6, and S7, the reductions in elastic properties caused by

different hydrous defects are not the same. The decrease in most elastic constants for Si2 hydrous Mgmj compared to dry Mgmj is larger than for Si1 hydrous Mgmj (Fig. S6) due to the different types of octahedrons they connect which leads to different magnitudes of volume changes, and it also directly results in a larger reduction of K and G than that of Si1 hydrous Mgmj (Fig. S7). As for Si3 hydrous Mgmj, the magnitudes of elastic constants are higher or lower than those of Si1 and Si2 hydrous Mgmj due to the combined effect of its intermediate bonding environment of two Mg and two Si octahedrons and different orientations of bonding structure (Fig. S6), which lead to a similar reduction of K and G with that of Si1 hydrous Mgmj (Fig. S7). This relative relationship of decrease in elastic modulus is carried through to seismic wave velocities because the decrease in density (e.g., about 1.59%, 1.15%, 0.97% for Si2 tetrahedron defect at 0 K and 0, 10, 20 GPa, respectively) is smaller than that in elastic moduli (> 2%, see Fig. S7). Based on these, the decrease in seismic velocities v_P and v_S caused by Si1 and Si3 hydrous defects, at the same water concentrations, are almost identical and smaller than those for Si2 hydrous defects (Fig. 5). The decrease in v_P and v_S caused by the three types of Si tetrahedron defects tend to decrease with increasing pressure. This is because higher pressure results in smaller volume changes, leading to smaller variations in the elastic constants as well as bulk and shear modulus which are carried through to the seismic wave speeds. Previous studies of the elasticity of high-pressure minerals (Mao & Li, 2016) indicate the linear relationship between the water concentration and the decreases in v_p and v_s. Based on this, the decrease of v_p and v_s caused by Si2 or Si3 hydrous defect with a general water concentration of Mgmj, i.e., ~700 ppm (Bolfan-Casanova et al., 2000; Katayama et al., 2003; Pigott et al., 2015), at 20 GPa are about 0.09% and 0.14% or 0.05% and 0.04%, respectively. Therefore, the differences in seismic wave velocities between dry and hydrous Mgmj are likely to be small in water-rich deep planetary regions, such as the MTZ in the Earth.

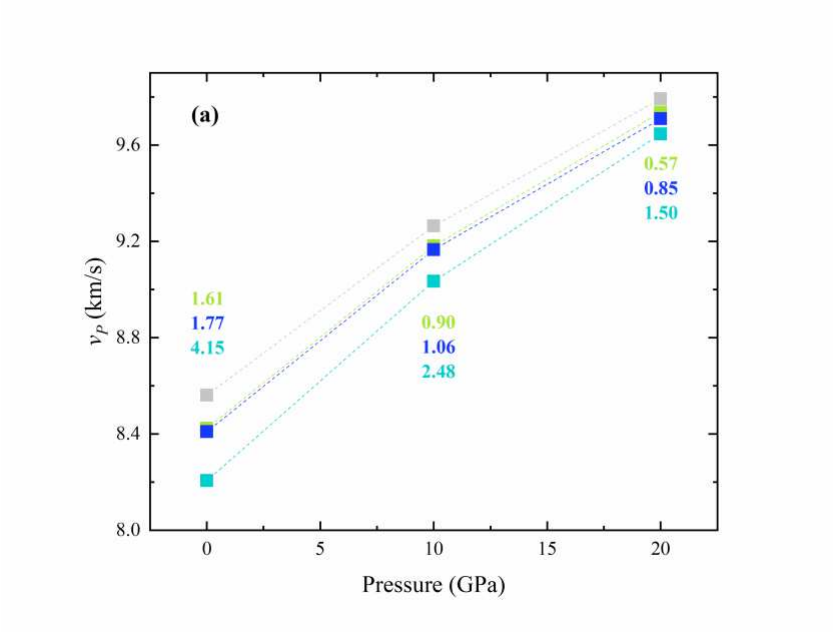

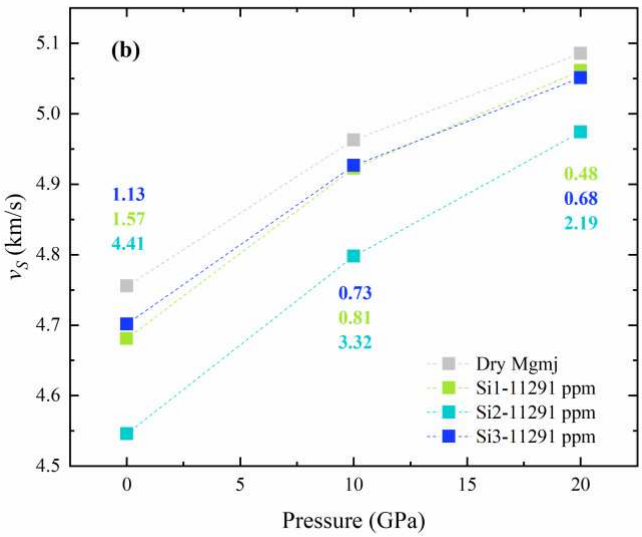

Figure 5. The variation of (a) v_P and (b) v_S caused by one Si1, Si2, and Si3 hydrous defect in Mgmj at 0 K. The colored numbers represent the percentage of decrease compared to dry Mgmj.

We further inspect the effects of hydrous defects on $R(H_2O)$, the ratio of $d\ln(v_S)/d(H_2O)$ and $d\ln(v_P)/d(H_2O)$, which is a useful tool to understand lateral heterogeneities in the planetary interiors (L. Li et al., 2011; Pigott et al., 2015). Here we calculated $R(H_2O)$ for Mgmj from:

$$R(H_2O) = \frac{\ln v_S(\text{hydrous}) - \ln v_S(\text{anhydrous})}{\ln v_P(\text{hydrous}) - \ln v_P(\text{anhydrous})} \quad (6)$$

Based on this formula, a large $R(H_2O)$ (> 1) indicates that v_S is more sensitive than v_P to the water concentration, whereas a small $R(H_2O)$ (< 1) means the opposite is true. As shown in Fig. 6, the $R(H_2O)$ of Mgmj seems to have no dependence on water concentration which indicated by the force field (classical atomistic simulations) data of Pigott et al. (2015) of hydrous Mgmj with Si2 hydrous defects, and our results for hydrous Mgmj with Mg3 and Si2 hydrous defects are in good agreement with their data. Since the Si3 hydrous defect is another major water incorporation mechanism, its $R(H_2O)$ was also calculated. The $R(H_2O)$ of Si2 and Si3 hydrous Mgmj are different, but both of them rise with increasing pressure. We also plotted the $R(H_2O)$ of wadsleyite and ringwoodite (the other two main minerals in the MTZ) using previous experimental and simulated data. Although both minerals are influenced by water concentration, their pressure-dependent trends are consistent: the $R(H_2O)$ of wadsleyite increases with pressure and remains greater than 1, whereas that of ringwoodite shows the opposite behavior. In comparison, the $R(H_2O)$ of Si2 hydrous Mgmj is closer to those of wadsleyite, while the $R(H_2O)$ of Si3 hydrous Mgmj is similar to those of ringwoodite at lower pressure but quite different at higher pressure. Since the dominance of these two defects, the $R(H_2O)$ of hydrous Mgmj will be between their individual values and reflects the ratio of the two defects which can be applied to some areas with high Mgmj content, such as cold subduction slab. Furthermore, the $R(H_2O)$ of Si2 hydrous Mgmj > 1 but those of Si3 < 1, there is a cancellation effect by $R(H_2O)$ of Si2 and Si3 hydrous Mgmj. To evaluate this, we also estimated the $R(H_2O)$ of hydrous Mgmj with a mixture of Si2 and Si3 hydrous defects in

412 a 1:1 ratio, because the proportion of Si3, which is about 50%, should be its upper limit due to the
413 weak pressure dependence of ratios of the hydrous defects and 2000K being the upper-temperature
414 limit of the MTZ. The values are calculated by presuming a linear relationship between water
415 concentration and seismic wave velocities (Mao & Li, 2016) and linear mixing of seismic wave
416 velocities between Si2 and Si3 hydrous Mgmj (Babuška et al., 1978; B. Li et al., 2022; Lou et al.,
417 2020). The results show that the $R(H_2O)$ is close to 1 at low pressure but larger than 1 at high
418 pressure. Based on this, we speculate that the decrease of v_S of Mgmj caused by water is larger
419 than that of v_P in MTZ. Therefore, the effect of water on lateral variations in seismic wave
420 velocities of Mgmj is more similar to wadsleyite, but different to ringwoodite. This property could
421 be used together with others, such as the relationship between temperature and elastic properties
422 of hydrous minerals, to study the compositional heterogeneities in hydration regions in deep
423 planetary interiors like the contact zone between subducting plates and the lower MTZ of the Earth.
424 It should be noted that the discussions above are deployed from static calculations, more high-
425 temperature and high-pressure elasticity studies of hydrous Mgmj may be required to see if this is
426 also true at high temperatures.

427 Studies of other hydrous garnet end-members are also required, to better understand the effect
428 of water on lateral variations in majoritic garnets. This is because water may affect the elastic
429 properties of different garnet endmembers in distinct ways, while the major elements (e.g., Fe, Ca,
430 and Al) also exert contrasting influences on the elasticity of majoritic garnet. Specifically, under
431 MTZ pressures, Fe reduces both v_P and v_S when comparing almandine with pyrope, whereas Ca
432 and Al increase them when comparing grossular with pyrope and pyrope with majorite-pyrope
433 garnet, respectively (Fig. 5b in Liu et al. (2019)). Regarding lateral heterogeneity in seismic wave
434 velocities, as shown in Fig. S8, Fe, Ca, and Al induce larger variations in v_S than in v_P under MTZ
435 pressures. In addition, there are several points deserve further considerations: (1) the Al-related
436 mechanisms of water incorporation, such as Al-H joint substitution for Si in octahedrons or
437 tetrahedrons, and a couple of substitutions of two Al for one Mg and one Si in polyhedrons; (2)
438 comprehensive studies of the effect of SiO_2 activity on our results. Our findings in this study should
439 be of value to extend to all these more realistic circumstances.

440

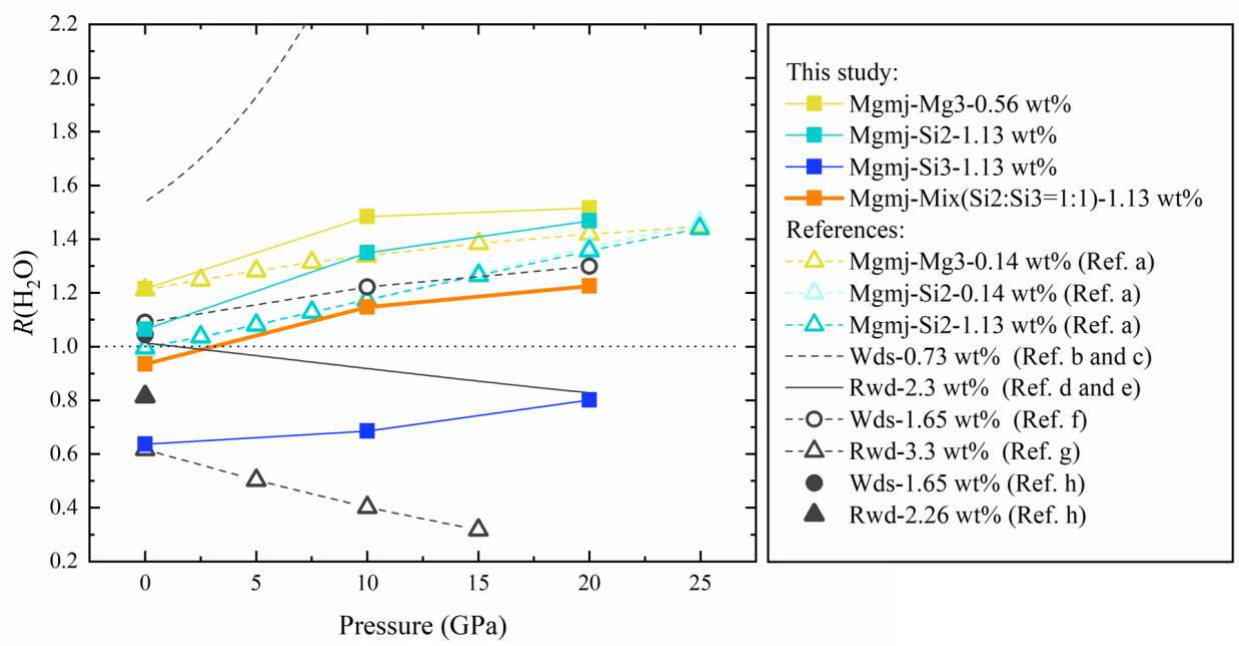

Figure 6. Comparisons of the $R(H_2O)$ of hydrous Mgmj and polymorphs of forsterite as a function of pressure. Ref. a: Pigott et al. (2015), static simulated data of Mgmj; Ref. b: Zha et al. (1997), experimental data only for dry wadsleyite at ambient temperature; Ref. c: Gwanmesia et al. (2020), experimental data only for hydrous wadsleyite at ambient temperature; Ref. d: B. Li (2003), experimental data only for dry ringwoodite at ambient temperature; Ref. e: Wang et al. (2006), experimental data only for hydrous ringwoodite at ambient temperature; Ref.f: Tsuchiya & Tsuchiya (2009), static simulated data of wadsleyite; Ref. g: Li et al. (2009), static simulated data of ringwoodite; Ref. h: Mao & Li (2016), ambient experimental data of wadsleyite and ringwoodite.

5 Conclusions

Our calculations provide insight into the water incorporation mechanisms in Mgmj and show that (1) the Si2 hydrous defect is dominant with almost no pressure dependence at 0 K, (2) Si2 and Si3 are the main hydrous defects with almost no dependence on water concentration at 2000 K and 20 GPa, and (3) these mechanisms are greatly affected by temperature. After evaluating the effect of the binding preferences of H^+ in defects, configurational entropy of mixed Mg hydrous defects, and the sensitivities of Mg1 hydrous defects to temperature and water concentration, Si2 and Si3 hydrous defects are demonstrated to be the main incorporation mechanisms of water in Mgmj under the Earth's and Mars' mantle conditions.

Our calculations also reveal the inequivalent effects of hydrous defects. The reductions of seismic wave velocities caused by the Si3 hydrous defect are about half of that of the Si2 hydrous defect under the same water concentration and pressure. The difference in seismic wave velocities between dry and hydrous Mgmj with dominant water incorporation mechanisms (Si2 and Si3 hydrous defects) and expected water concentration (~700 ppm) are likely to be small (on the order of one ten-thousandth). We also find that the effect of water on ν_S of Mgmj is larger than that of ν_P based on the $R(H_2O)$. Since the effect of water on lateral variations of seismic wave velocities in Mgmj is opposite to that in ringwoodite, their $R(H_2O)$ could be potential tools to discriminate compositional heterogeneities in some hydration regions such as the contact zone between subducting plates and the lower MTZ. Since the findings about elastic properties come from static calculations, thus, more high-temperature and high-pressure elasticity studies of hydrous Mgmj are required to see if this is also true at high temperatures. Studies of other hydrous garnet end-members are also required, to better understand the effect of water on lateral variations in majoritic garnets. In addition, there are several points we don't consider or investigate in detail in this study: (1) the Al-related mechanisms of water incorporation, such as Al-H joint substitution for Si in octahedrons or tetrahedrons, and a couple of substitutions of two Al for one Mg and one Si in polyhedrons; (2) comprehensive studies of the effect of SiO_2 activity on our results. Finally, this study provides inspiration and reference for the investigation of the partitioning of water between high-pressure minerals, which can provide insights into the deep Earth water cycle by examining how water is distributed among minerals in different layers of the Earth's interior, and our findings in this study should be of value to extend to all these more realistic circumstances.

Acknowledgments

This work was supported by the National Key R&D Program of China (Grant 2022YFF0503203 and 2018YFA0702700), the key research program of IGGCAS (IGGCAS-202204), the Guangdong S&T Program (2024B0303390002), the National Natural Science Foundation of China (grant 92462303), the Strategic Priority Research Program of the Chinese Academy of Sciences (grant XDA0430205), the Deep Earth Probe and Mineral Resources Exploration —— National Science and Technology Major Project of China (2024ZD1004002, J.Z.), the National Key R&D Program of China (grant 2021YFC2901701), and the Science and Technology Planning of Guangdong Province, China (grant 2023B1212060048). Simulations were carried out on the computational facilities in the Computer Simulation Lab of IGGCAS and Tianhe-2 at the National Supercomputer Center of China (NSCC) in Guangzhou. The collaboration leading to this paper was made possible by the U.K.-Sino Centre for Earth and Planetary Science.

Data Availability Statement

The Vienna ab initio simulation package (VASP, Kresse & Furthmüller, 1996a, 1996b) is available under the VASP license at https://www.vasp.at/. An open-source visualization software VESTA (Momma & Izumi, 2011) used to show the crystal structures (Fig. 1 and 4) is available under the VESTA license at https://jp-minerals.org/vesta/en/. All the data used in this study have been deposited at Lou (2025).

Conflict of Interest

The authors declare that they have no conflict of interest.

References

Adhikari, P., Dharmawardhana, C. C., & Ching, W.-Y. (2017). Structure and properties of hydrogrossular mineral series. *Journal of the American Ceramic Society*, *100*(9), 4317–4330. https://doi.org/10.1111/jace.14970

Akaogi, M., & Akimoto, S. -i. (1977). Pyroxene-garnet solid-solution equilibria in the systems Mg4Si4O12 Mg3Al2Si3O12 and Fe4Si4O12 Fe3Al2Si3O12 at high pressures and temperatures. *Physics of the Earth and Planetary Interiors*, *15*(1), 90–106.

Angel, R. J., Finger, L. W., Hazen, R. M., Kanzaki, M., Weidner, D. J., Liebermann, R. C., & Veblen, D. R. (1989). Structure and twinning of single-crystal MgSiO3 garnet synthesized at 17 GPa and 1800 C. *American Mineralogist: Journal of Earth and Planetary Materials*, *74*(3–4), 509–512.

Babuška, V., Fiala, J., Kumazawa, M., Ohno, I., & Sumino, Y. (1978). Elastic properties of garnet solid-solution series. *Physics of the Earth and Planetary Interiors*, *16*(2), 157–176. https://doi.org/10.1016/0031-9201(78)90086-9

Balan, E., Ingrin, J., Delattre, S., Kovács, I., & Blanchard, M. (2011). Theoretical infrared spectrum of OH-defects in forsterite. *European Journal of Mineralogy*, *23*(3), 285–292. https://doi.org/10.1127/0935-1221/2011/0023-2090

Bell, D. R., & Rossman, G. R. (1992). Water in Earth's mantle: The role of nominally anhydrous minerals. *Science*, *255*(5050), 1391–1397.

Blanchard, M., Balan, E., & Wright, K. (2009). Incorporation of water in iron-free ringwoodite: A first-principles study. *American Mineralogist*, *94*(1), 83–89.

Blöchl, P. E. (1994). Projector augmented-wave method. *Physical Review B*, *50*(24), 17953.

529 Bolfan-Casanova, N. (2005). Water in the Earth's mantle. *Mineralogical Magazine*, *69*(3), 229–
530 257.
531 Bolfan-Casanova, N., Keppler, H., & Rubie, D. C. (2000). Water partitioning between nominally
532 anhydrous minerals in the MgO–SiO2–H2O system up to 24 GPa: Implications for the
533 distribution of water in the Earth's mantle. *Earth and Planetary Science Letters*, *182*(3–
534 4), 209–221.
535 Cohen-Addad, C., Ducros, P., & Bertaut, E. F. (1967). Étude de la substitution du groupement
536 SiO4 par (OH) 4 dans les composés Al2Ca3 (OH) 12 et Al2Ca3 (SiO4) 2, 16 (OH) 3, 36
537 de type grenat. *Acta Crystallographica*, *23*(2), 220–230.
538 Faccenda, M. (2014). Water in the slab: A trilogy. *Tectonophysics*, *614*, 1–30.
539 https://doi.org/10.1016/j.tecto.2013.12.020
540 Frost, D. J. (2008). The upper mantle and transition zone. *Elements*, *4*(3), 171–176.
541 Geiger, C. A., Langer, K., Bell, D. R., Rossman, G. R., & Winkler, B. (1991). The hydroxide
542 component in synthetic pyrope. *American Mineralogist*, *76*(1–2), 49–59.
543 Geiger, C. A., Stahl, A., & Rossman, G. R. (2000). Single-crystal IR-and UV/VIS-spectroscopic
544 measurements on transition-metal-bearing pyrope: The incorporation of hydroxide in
545 garnet. *European Journal of Mineralogy*, *12*(2), 259–271.
546 Grimme, S., Antony, J., Ehrlich, S., & Krieg, H. (2010). A consistent and accurate ab initio
547 parametrization of density functional dispersion correction (DFT-D) for the 94 elements
548 H-Pu. *The Journal of Chemical Physics*, *132*(15).
549 https://pubs.aip.org/aip/jcp/article/132/15/154104/926936
550 Gwanmesia, G. D., Whitaker, M. L., Dai, L., James, A., Chen, H., Triplett, R. S., & Cai, N.
551 (2020). The Elastic Properties of β-Mg2SiO4 Containing 0.73 wt.% of H2O to 10 GPa

552 and 600 K by Ultrasonic Interferometry with Synchrotron X-Radiation. *Minerals*, *10*(3),
553 209. https://doi.org/10.3390/min10030209
554 Hazen, R. M. (1976). Effects of temperature and pressure on the crystal structure of forsterite.
555 *American Mineralogist*, *61*(11–12), 1280–1293.
556 Hirschmann, M., & Kohlstedt, D. (2012). Water in Earth's mantle. *Physics Today*, *65*(3), 40–45.
557 Hohenberg, P., & Kohn, W. (1964). Inhomogeneous electron gas. *Physical Review*, *136*(3B),
558 B864.
559 Inoue, T., Weidner, D. J., Northrup, P. A., & Parise, J. B. (1998). Elastic properties of hydrous
560 ringwoodite (γ-phase) in Mg2SiO4. *Earth and Planetary Science Letters*, *160*(1–2), 107–
561 113.
562 Irifune, T. (1987). An experimental investigation of the pyroxene-garnet transformation in a
563 pyrolite composition and its bearing on the constitution of the mantle. *Physics of the*
564 *Earth and Planetary Interiors*, *45*(4), 324–336.
565 Irifunea, T., & Ringwood, A. E. (1987). Phase transformations in primitive MORB and pyrolite
566 compositions to 25 GPa and some geophysical implications. In M. H. Manghnani & Y.
567 Syono (Eds.), *Geophysical Monograph Series* (Vol. 39, pp. 231–242). American
568 Geophysical Union. https://doi.org/10.1029/GM039p0231
569 Jacobsen, S. D., Holl, C. M., Adams, K. A., Fischer, R. A., Martin, E. S., Bina, C. R., Lin, J.-F.,
570 Prakapenka, V. B., Kubo, A., & Dera, P. (2008). Compression of single-crystal
571 magnesium oxide to 118 GPa and a ruby pressure gauge for helium pressure media.
572 *American Mineralogist*, *93*(11–12), 1823–1828.

573 Jacobsen, S. D., Jiang, F., Mao, Z., Duffy, T. S., Smyth, J. R., Holl, C. M., & Frost, D. J. (2008).
574 Effects of hydration on the elastic properties of olivine. *Geophysical Research Letters*,
575 *35*(14).
576 Katayama, I., Hirose, K., Yurimoto, H., & Nakashima, S. (2003). Water solubility in majoritic
577 garnet in subducting oceanic crust. *Geophysical Research Letters*, *30*(22).
578 Kohn, W., & Sham, L. J. (1965). Self-consistent equations including exchange and correlation
579 effects. *Physical Review*, *140*(4A), A1133.
580 Kresse, G., & Furthmüller, J. (1996a). Efficiency of ab-initio total energy calculations for metals
581 and semiconductors using a plane-wave basis set. *Computational Materials Science*, *6*(1),
582 15–50.
583 Kresse, G., & Furthmüller, J. (1996b). Efficient iterative schemes for ab initio total-energy
584 calculations using a plane-wave basis set. *Physical Review B*, *54*(16), 11169.
585 Kresse, G., & Hafner, J. (1993). Ab initio molecular dynamics for liquid metals. *Physical Review*
586 *B*, *47*(1), 558.
587 Kresse, G., & Joubert, D. (1999). From ultrasoft pseudopotentials to the projector augmented-
588 wave method. *Physical Review B*, *59*(3), 1758.
589 Lemaire, C., Kohn, S. C., & Brooker, R. A. (2004). The effect of silica activity on the
590 incorporation mechanisms of water in synthetic forsterite: A polarised infrared
591 spectroscopic study. *Contributions to Mineralogy and Petrology*, *147*, 48–57.
592 Levien, L., Prewitt, C. T., & Weidner, D. J. (1980). Structure and elastic properties of quartz at
593 pressure. *American Mineralogist*, *65*(9–10), 920–930.
594 Levine, I. N. (2009). *Physical chemistry* (6th ed). McGraw-Hill.

595 Li, B. (2003). Compressional and shear wave velocities of ringwoodite γ-Mg2SiO4 to 12 GPa.
596 *American Mineralogist*, *88*(8–9), 1312–1317. https://doi.org/10.2138/am-2003-8-913
597 Li, B., Jiang, J., Xu, J., Tkachev, S. N., Ye, Z., Huang, S., Guo, W., Zeng, Y., Prakapenka, V. B.,
598 Fan, D., & Zhou, W. (2022). Effect of Thermoelastic Properties of the Pyrope-Almandine
599 Solid Solutions on the Entrapment Pressure of Garnet-Related Elastic Geobarometer.
600 *Frontiers in Earth Science*, *9*.
601 https://www.frontiersin.org/articles/10.3389/feart.2021.833405
602 Li, L., Brodholt, J., & Alfè, D. (2009). Structure and elasticity of hydrous ringwoodite: A first
603 principle investigation. *Physics of the Earth and Planetary Interiors*, *177*(3–4), 103–115.
604 Li, L., Weidner, D. J., Brodholt, J. P., & Alfè, D. (2011). Prospecting for water in the transition
605 zone: D ln (Vs)/d ln (Vp). *Physics of the Earth and Planetary Interiors*, *189*(1–2), 117–
606 120.
607 Liu, Z., Gréaux, S., Cai, N., Siersch, N., Ballaran, T. B., Irifune, T., & Frost, D. J. (2019).
608 Influence of aluminum on the elasticity of majorite-pyrope garnets. *American*
609 *Mineralogist*, *104*(7), 929–935. https://doi.org/10.2138/am-2019-6771
610 Lou, Y. (2025). *Water Incorporation Mechanisms and Effects in MgSiO3-majorite Under High*
611 *Temperature and Pressure Conditions* [Dataset].
612 https://doi.org/10.5281/zenodo.17406948
613 Lou, Y., Stackhouse, S., Walker, A. M., & Zhang, Z. (2020). Thermoelastic properties of
614 MgSiO3-majorite at high temperatures and pressures: A first principles study. *Physics of*
615 *the Earth and Planetary Interiors*, *303*, 106491.
616 https://doi.org/10.1016/j.pepi.2020.106491

617 Manghnani, M. H., Amulele, G., Smyth, J. R., Holl, C. M., Chen, G., Prakapenka, V., & Frost,
618 D. J. (2005). Equation of state of hydrous Fo90 ringwoodite to 45 GPa by synchrotron
619 powder diffraction. *Mineralogical Magazine*, *69*(3), 317–323.
620 Mao, Z., Jacobsen, S. D., Frost, D. J., McCammon, C. A., Hauri, E. H., & Duffy, T. S. (2011).
621 Effect of hydration on the single-crystal elasticity of Fe-bearing wadsleyite to 12 GPa.
622 *American Mineralogist*, *96*(10), 1606–1612.
623 Mao, Z., & Li, X. (2016). Effect of hydration on the elasticity of mantle minerals and its
624 geophysical implications. *Science China Earth Sciences*, *59*, 873–888.
625 Matveev, S., O'neill, H. S. C., Ballhaus, C., Taylor, W. R., & Green, D. H. (2001). Effect of
626 silica activity on OH- IR spectra of olivine: Implications for low-a SiO2 mantle
627 metasomatism. *Journal of Petrology*, *42*(4), 721–729.
628 Momma, K., & Izumi, F. (2011). VESTA 3 for three-dimensional visualization of crystal,
629 volumetric and morphology data. *Journal of Applied Crystallography*, *44*(6), 1272–1276.
630 https://doi.org/10.1107/S0021889811038970
631 Muir, J. M. R., & Brodholt, J. P. (2018). Water distribution in the lower mantle: Implications for
632 hydrolytic weakening. *Earth and Planetary Science Letters*, *484*, 363–369.
633 https://doi.org/10.1016/j.epsl.2017.11.051
634 Nestola, F., & Smyth, J. R. (2016). Diamonds and water in the deep Earth: A new scenario.
635 *International Geology Review*, *58*(3), 263–276.
636 https://doi.org/10.1080/00206814.2015.1056758
637 Ni, H., Zheng, Y.-F., Mao, Z., Wang, Q., Chen, R.-X., & Zhang, L. (2017). Distribution, cycling
638 and impact of water in the Earth's interior. *National Science Review*, *4*(6), 879–891.
639 https://doi.org/10.1093/nsr/nwx130

Nosé, S. (1984). A molecular dynamics method for simulations in the canonical ensemble. *Molecular Physics*, *52*(2), 255–268.

Ohtani, E. (2020). The role of water in Earth's mantle. *National Science Review*, *7*(1), 224–232.

Pearson, D. G., Brenker, F. E., Nestola, F., McNeill, J., Nasdala, L., Hutchison, M. T., Matveev, S., Mather, K., Silversmit, G., Schmitz, S., Vekemans, B., & Vincze, L. (2014). Hydrous mantle transition zone indicated by ringwoodite included within diamond. *Nature*, *507*(7491), Article 7491. https://doi.org/10.1038/nature13080

Perdew, J. P., Burke, K., & Ernzerhof, M. (1996). Generalized gradient approximation made simple. *Physical Review Letters*, *77*(18), 3865.

Peslier, A. H., Schönbächler, M., Busemann, H., & Karato, S.-I. (2017). Water in the Earth's Interior: Distribution and Origin. *Space Science Reviews*, *212*(1), 743–810. https://doi.org/10.1007/s11214-017-0387-z

Pigott, J. S., Wright, K., Gale, J. D., & Panero, W. R. (2015). Calculation of the energetics of water incorporation in majorite garnet. *American Mineralogist*, *100*(5–6), 1065–1075.

Qin, T., Wentzcovitch, R. M., Umemoto, K., Hirschmann, M. M., & Kohlstedt, D. L. (2018). Ab initio study of water speciation in forsterite: Importance of the entropic effect. *American Mineralogist*, *103*(5), Article 5.

Ringwood, A. E. (1967). The pyroxene-garnet transformation in the earth's mantle. *Earth and Planetary Science Letters*, *2*(3), 255–263.

Ringwood, A. E. (1991). Phase transformations and their bearing on the constitution and dynamics of the mantle. *Geochimica et Cosmochimica Acta*, *55*(8), 2083–2110.

Ross, N. L., Shu, J., & Hazen, R. M. (1990). High-pressure crystal chemistry of stishovite. *American Mineralogist*, *75*(7–8), 739–747.

663 Rossman, G. R., & Aines, R. D. (1991). The hydrous components in garnets: Grossular-
664 hydrogrossular. *American Mineralogist*, *76*(7–8), 1153–1164.
665 Scambelluri, M., Pettke, T., & van Roermund, H. L. M. (2008). Majoritic garnets monitor deep
666 subduction fluid flow and mantle dynamics. *Geology*, *36*(1), 59–62.
667 https://doi.org/10.1130/G24056A.1
668 Smith, E. M., Shirey, S. B., Richardson, S. H., Nestola, F., Bullock, E. S., Wang, J., & Wang, W.
669 (2018). Blue boron-bearing diamonds from Earth's lower mantle. *Nature*, *560*(7716), 84–
670 87. https://doi.org/10.1038/s41586-018-0334-5
671 Smyth, J. R., & Jacobsen, S. D. (2006). Nominally anhydrous minerals and Earth's deep water
672 cycle. *Earth's Deep Water Cycle*, *168*, 1–11.
673 Stixrude, L., & Lithgow-Bertelloni, C. (2012). Geophysics of Chemical Heterogeneity in the
674 Mantle. *Annual Review of Earth and Planetary Sciences*, *40*(1), 569–595.
675 https://doi.org/10.1146/annurev.earth.36.031207.124244
676 Thomas, S.-M., Wilson, K., Koch-Müller, M., Hauri, E. H., McCammon, C., Jacobsen, S. D.,
677 Lazarz, J., Rhede, D., Ren, M., & Blair, N. (2015). Quantification of water in majoritic
678 garnet. *American Mineralogist*, *100*(5–6), 1084–1092.
679 Tkatchenko, A., & Scheffler, M. (2009). Accurate Molecular Van Der Waals Interactions from
680 Ground-State Electron Density and Free-Atom Reference Data. *Physical Review Letters*,
681 *102*(7), 073005. https://doi.org/10.1103/PhysRevLett.102.073005
682 Tsuchiya, J., & Tsuchiya, T. (2009). First principles investigation of the structural and elastic
683 properties of hydrous wadsleyite under pressure. *Journal of Geophysical Research: Solid*
684 *Earth*, *114*(B2).

van der Lee, S. (2023). Deep Mars is surprisingly soft. *Nature*, *622*(7984), 699–700. https://doi.org/10.1038/d41586-023-03151-x

van Mierlo, W. L., Langenhorst, F., Frost, D. J., & Rubie, D. C. (2013). Stagnation of subducting slabs in the transition zone due to slow diffusion in majoritic garnet. *Nature Geoscience*, *6*(5), 400–403. https://doi.org/10.1038/ngeo1772

Walker, A. M., Hermann, J., Berry, A. J., & O'Neill, H. S. C. (2007). Three water sites in upper mantle olivine and the role of titanium in the water weakening mechanism. *Journal of Geophysical Research: Solid Earth*, *112*(B5).

Wang, J., Sinogeikin, S. V., Inoue, T., & Bass, J. D. (2006). Elastic properties of hydrous ringwoodite at high-pressure conditions. *Geophysical Research Letters*, *33*(14).

Wright, K., Freer, R., & Catlow, C. R. A. (1994). The energetics and structure of the hydrogarnet defect in grossular: A computer simulation study. *Physics and Chemistry of Minerals*, *20*(7), 500–503. https://doi.org/10.1007/BF00203220

Ye, Y., Brown, D. A., Smyth, J. R., Panero, W. R., Jacobsen, S. D., Chang, Y.-Y., Townsend, J. P., Thomas, S.-M., Hauri, E. H., & Dera, P. (2012). Compressibility and thermal expansion of hydrous ringwoodite with 2.5 (3) wt% H2O. *American Mineralogist*, *97*(4), 573–582.

Yoshizaki, T., & McDonough, W. F. (2020). The composition of Mars. *Geochimica et Cosmochimica Acta*, *273*, 137–162. https://doi.org/10.1016/j.gca.2020.01.011

Yoshizaki, T., & McDonough, W. F. (2021). Earth and Mars – Distinct inner solar system products. *Geochemistry*, *81*(2), 125746. https://doi.org/10.1016/j.chemer.2021.125746

706 Zha, C., Duffy, T. S., Mao, H., Downs, R. T., Hemley, R. J., & Weidner, D. J. (1997). Single-
707 crystal elasticity of β-Mg2SiO4 to the pressure of the 410 km seismic discontinuity in the
708 earth's mantle. *Earth and Planetary Science Letters*, *147*(1–4), E9–E15.
709 Zhang, B., & Xia, Q. (2021). Influence of water on the physical properties of olivine, wadsleyite,
710 and ringwoodite. *European Journal of Mineralogy*, *33*(1), 39–75.
711 https://doi.org/10.5194/ejm-33-39-2021
712 Zhang, Z., Stixrude, L., & Brodholt, J. (2013). Elastic properties of MgSiO3-perovskite under
713 lower mantle conditions and the composition of the deep Earth. *Earth and Planetary*
714 *Science Letters*, *379*, 1–12.

715
716